Rayleigh to Love wave conversion in a mountain root structure

Mitsuru Yoshida*

Earthquake Research Institute, University of Tokyo

Abstract

Surface wave interconversion in the Tien Shan-like mountain range was investigated through numerical seismic wave simulations by the use of the 3-D finite difference method. The Tien Shan, located in the western part of the Lop Nor nuclear test site in China, is a candidate region where conversion from Rayleigh to Love wave occurs. Striking features of the mountain model analyzed include the existence of a large-scale double low velocity zone (LVZ) in the crust and in the upper mantle beneath the mountain. Simulation results for the oblique incidence of an azimuth of 60 deg. on the mountain range show that the spectral amplitude levels of converted Love waves are at most 0.3–0.4 of those of Rayleigh waves of the vertical component. These amplitudes of converted Love waves are too low to explain observed strong Love waves (Pedersen *et al.,* 1998) due to the Chinese nuclear test at Lop Nor. The results suggest that the observed large amplitudes of Love waves might be generated by the amplification of converted Love waves due to the complicated geometry of the Tien Shan, which is not taken into consideration in the present model and/or the tectonic release near the nuclear test site. If we evaluate wave energy from the sum of squares of amplitudes of wavetrains, it is suggested that the wave energy of converted Love waves at the wave's approach site of the mountain is relatively higher than that at the wave's retreat site of the mountain in the eastern Tien Shan, while the situation is reversed in the western Tien Shan. For the mountain model without the LVZ, the energy of converted Love waves at the retreat site is much higher than that at the wave's approach site in both the eastern and the western Tien Shan.

Key words: Rayleigh wave, converted Love wave, rate of conversion, wave energy

1. Introduction

In the propagation of seismic surface waves in media with strong lateral heterogeneity in the transverse direction, interconversions between Rayleigh and Love waves are likely to occur. For media with a vertical discontinuity, mode conversion from Rayleigh to Love waves was investigated by Malishewsky (1976) and Gregersen (1978). They presented the angular dependence of the reflection and the transmission coefficients for surface waves that are obliquely incident at a vertical discontinuity. The interconversion between Rayleigh and Love waves in mountain root structures was studied by Pedersen *et al.* (1998). On the other hand, when surface waves encounter a lateral heterogeneity they may generate outgoing radiation fields, or body waves. The radiation mode has been investigated from the viewpoints of wave energy (Momoi, 1987), reflection and transmission coefficients (Malishewsky, 1987, 2000), eigenfuctions (Maupin, 1996), and spatio-temporal distributions of amplitude and phase (Yoshida, 1999).

It is pointed out by Pedersen *et al.* (1998, Fig. 3) that strong Love waves are observed from the Chines nuclear test at Lop Nor, and the high conversion from Rayleigh to Love waves might be caused in the Tien Shan region. They showed that the rate of conversion is increased by the introduction of the topography of Moho and a low velocity zone (LVZ) in the lower crust. The rate of conversion, however, is not sufficient to quantitatively explain

* e-mail: mitsuru@eri.u-tokyo.ac.jp (1–1–1, Yayoi, Bunkyo-ku, Tokyo, 113–0032 Japan)

the large amplitudes of Love waves (Pedersen *et al.* (1998, Fig. 15)). Although crustal models of the Tien Shan are presented by several authors (e.g., Burov *et al.,* 1990; Avouac *et al.,* 1993; Kosarev *et al.,* 1993), the existence of the LVZ in the upper mantle is indicated by Cotton and Avouac (1994) from analyses of surface wave group velocities.

The response function of oscillations of a mountain root structure similar to the Tien Shan, due to Rayleigh wave incidence, was investigated by Yoshida (2001: paper I). Paper I made clear in 2-D simulations that the existence of a large-scale double LVZ beneath the mountain range brings about large differences in amplitude response between the vertical and radial components. The present paper investigates whether or not the high rate of conversion from Rayleigh to Love waves can be realized if we introduce the large-scale double LVZ in both the crust and the upper mantle. The problem of the oblique incidence of plane Rayleigh waves on an irregular front of a Tien Shan-like mountain is investigated by the use of the 3-D finite difference method. The variation of wave energy between incident and transmitted waves is also elucidated.

2. Equation of motion and numerical models

The 3-D finite difference method can be applied in the complete elastic wave field in a medium having a complicated velocity structure, including surface-to-body wave conversion, diffraction, and multiple scattering (Frankel and Vidale, 1992; Yomogida and Etgen, 1993). Let U, V, W be the displacements in the x, y, z directions, respectively. For 3-D laterally inhomogeneous media, the basic equation for the three coupled waves is:

$$\rho U_{tt} = [(\lambda+2\mu)U_x+\lambda V_y+\lambda W_z]_x + [\mu U_y+\mu V_x]_y$$
$$+ [\mu U_z+\mu W_x]_z,$$
$$\rho V_{tt} = [(\lambda+2\mu)V_y+\lambda W_z+\lambda U_x]_y + [\mu V_z+\mu W_y]_z$$
$$+ [\mu V_x+\mu U_y]_x,$$
$$\rho W_{tt} = [(\lambda+2\mu)W_z+\lambda U_x+\lambda V_y]_z + [\mu W_x+\mu U_z]_x$$
$$+ [\mu W_y+\mu V_z]_y. \tag{1}$$

Here, ρ denotes density and λ and μ are the Lame' constants. Subscripts denote partial derivatives. These medium properties vary with position, and the medium is assumed to be isotropic.

The boundary conditions on the free surface at z =0 (Mikumo *et al.,* 1987; Chang and McMechan, 1989) are that normal stress is zero:

$$P_{zz} = \lambda(U_x+V_y+W_z)+2\mu W_z = 0, \tag{2}$$

and tangential stress is zero:

$$P_{zx} = \mu(W_x+U_z) = 0,$$
$$P_{yz} = \mu(V_z+W_y) = 0. \tag{3}$$

The partial derivatives are replaced by their finite difference approximations for a 3-D grid with equal spacing ($\Delta h = 5$ km) in the x, y, and z directions. The time increment ($\Delta t = 0.3$ s) satisfies the stability conditions:

$$\Delta t < \Delta h / \sqrt{\alpha^2+\beta^2}, \tag{4}$$

where α and β are the maximum compressional and shear wave velocities:

$$\alpha = \sqrt{(\lambda+2\mu)/\rho}, \tag{5}$$

and

$$\beta = \sqrt{\mu/\rho}. \tag{6}$$

The A1 absorption boundary condition (Clayton and Engquist, 1977), a zero order paraxial approximation for artificial reflection, was applied at the computational sides and at the bottom. The spatial increment is less than one-tenth of the wavelength to avoid the grid dispersion (Aki and Richard, 1980).

A brief sketch of the oblique incidence of plane Rayleigh waves on the irregular front (t1) of the mountain root structure is shown in Fig. 1. The background stratified medium consists of upper and lower crusts overlying a homogeneous mantle. The depths of the upper and lower crusts are 22.5 and 37.5 km, respectively. In the mountain root structure (Model T) the horizontal width of the mountain root between sites 5 and 15 is assumed to be 250 km. The horizontal lengths of sloping layers, located at both sides of sites 5 and 15, are 100 km. The bottom of the mountain root is located at the central part with a horizontal length of 50 km in the 2-D structure. Site 10 is locatd at a mid-point of the mountain root. The maximum depths of the upper and lower crusts of the mountain root are 37.5 and 52.5 km, respectively. In the mountain root structure with a large-scale double LVZ beneath the mountain (Model LB), the first and second LVZs are located at depths of 37.5–52.5 km and 112.5–162.5 km between sites 5 and 15, respectively. The physical parameters (α, β, ρ) for the upper and lower crusts and the upper mantle are (6.5 km/s, 3.9 km/s, 2.6 Mg/m^3), (7.0 km/s, 4.0 km/s, 2.75 Mg/m^3), and (7.9 km/s, 4.9 km/s, 3.35 Mg/m^3), respectively, Similaly, each parameter of the first and second LVZs is (6.5km/s, 3.5 km/s, 2.60 Mg/m^3) and (7.3789 km/s, 4.3433 km/s, 3.1012 Mg/m^3), respectively.
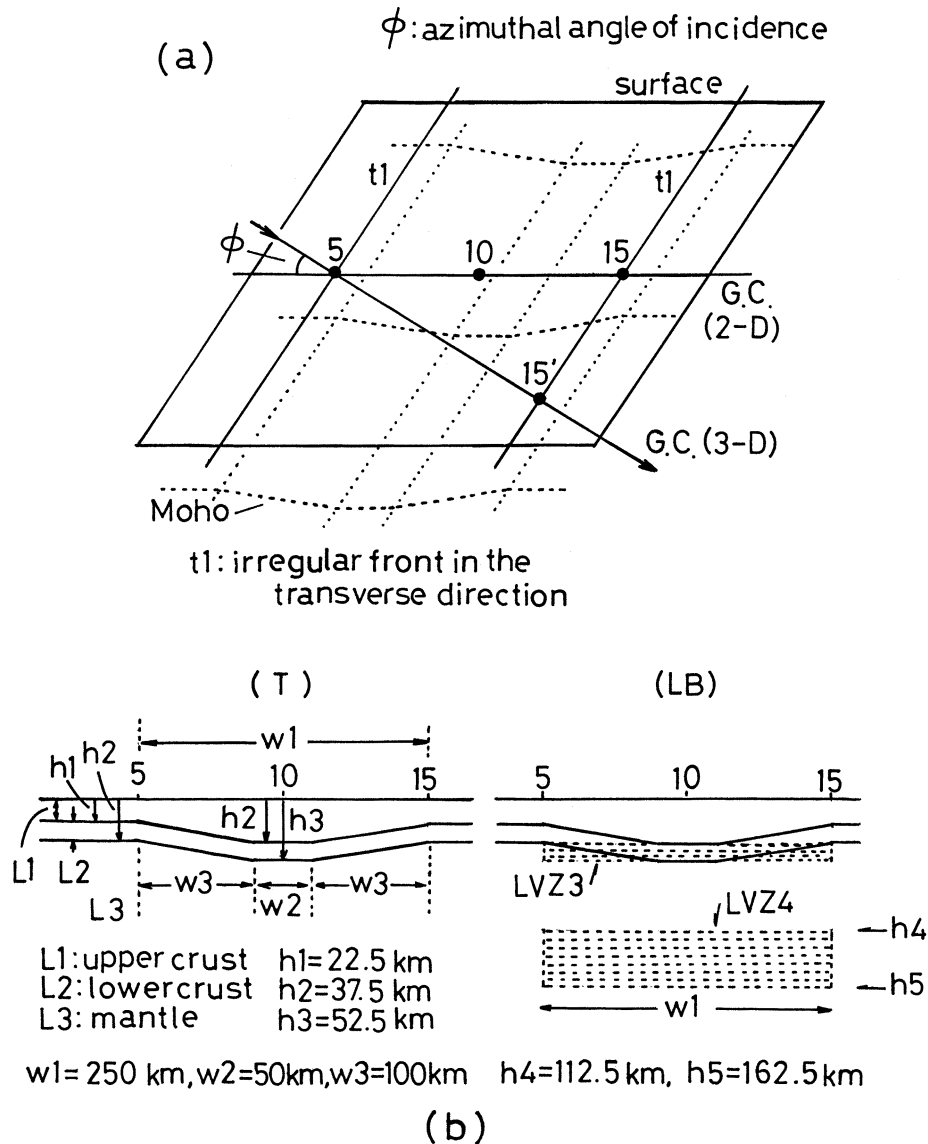
Fig. 1.(a) A bird's eye view of the oblique incidence of plane Rayleigh waves on the irregular front (t1) of the mountain root structure. Waves are incoming from the left (site 5) and are outgoing to the right. Waves travel towards site 15 or 15′ along a great circle (G.C.) path for the 2-D or 3-D model, respectively. In the 2-D model, the waves are incident on site 5 with $\phi=0$ deg., normal to t1. The distances between sites 5 and 15′ for the 3-D model with azimuthal angles of incidence of $\phi=30$ and 60 degs. are 290 and 500 km, respectively. Site 10 is located at the mid-point of the mountain root structure in the 2-D model. (b) Schematic map showing the 2-D crustal and upper mantle structures with (Model LB) and without (Model T) a double low velocity zone (LVZ) beneath the mountain. The depths of upper (L1) and lower (L2) crusts extend to 22.5 km (h1) and 37.5 km (h2), respectively. In Model T the width (w1) of a mountain root is assumed to be 250 km, and the horizontal lengths of sloping layer (w3) and bottom (w2) 100 and 50 km, respectively. The bottom (h3) of the mountain root is located at a depth of 52.5 km.

The layer parameters for the stratified medium and the mountain root structure are similar to those of the Tien Shan region (Kosarev *et al.,* 1993), based on body wave data. The parameters for the second LVZ are adopted from those of Cotton and Avouac (1994), based on surface wave data.

In the 2-D mountain root structure incident plane Rayleigh waves travel along a great circle (G. C.) on which sites 5, 10, and 15 are located (see Fig. 1). In 3-D media, the mountain root structure is extended transversely (y-axis) and the waves are incoming from the left (site 5) with an azimuthal angle

of incidence of ϕ, and are outgoing along a great circle on which site 15′ is located. The distance between sites 5 and 15′ for $\phi = 30°$ and 60° are 290 and 500 km, respectively. In the 2-D model, the waves are incident on site 5 with $\phi = 0°$. 3-D model calculations were done for two cases of $\phi = 30°$ and 60°. The computational space has horizontal lengths of 2100 and 2200 km in the x- and y-directions, respectively, and a vertical length of 600 km in the z-direction. The total number of grids in the x-, y-, and z-directions is 421, 441, and 122, respectively. Initial values (Boore, 1970) are given by

$$(W)_{t=0} = h(x, y, z), \tag{7}$$
$$(\partial W/\partial t)_{t=0} = i(x, y, z),$$

for the W-component and

$$(U)_{t=0} = j(x, y, z), \tag{8}$$
$$(\partial U/\partial t)_{t=0} = k(x, y, z),$$

for the U-component, where h (x, y, z), i (x, y, z), j (x, y, z), and k (x, y, z) are determined from normal mode solutions for the stratified medium located at the left side of site 5. The initial values, which were determined by paper I for spheroidal oscillations, assuming a dip-slip point source and a step function in time as a seismic source, were used. The seismic moment was temporarily assumed to be $1.0 + E26$ dyne·cm. The waves correspond to the fundamental mode Rayleigh waves excited at a point with a focal depth of 10.3 km, at the azimuth of 90° as measured counter-clockwise from the fault strike, with the shortest epicentral distance of 100 km (left edge of the computational space) and the longest one 600 km, and with a travel time of 92.21 s (the time $t = 0$ in Eqs. (7) and (8)). The spectra of incident Rayleigh waves show following frequency characteristics (Fig. 2 a) that spectral peaks of both the W- and the U-components are located at 23 s (0.043 Hz) and the amplitudes of the W-component are larger than those of the U-component in a period range of 16–100 s (0.01–0.063 Hz). The spectra are obtained using Rayleigh waves at site 5, simulated for the 3-D stratified medium (Model S).

3. Characteristics of spectra of converted Love waves

Fourier spectra of transmitted waves are determined in order to compare the spectral characteristic of the V-component with those of the W- and the U-components. Wavetrains incident on the moun-
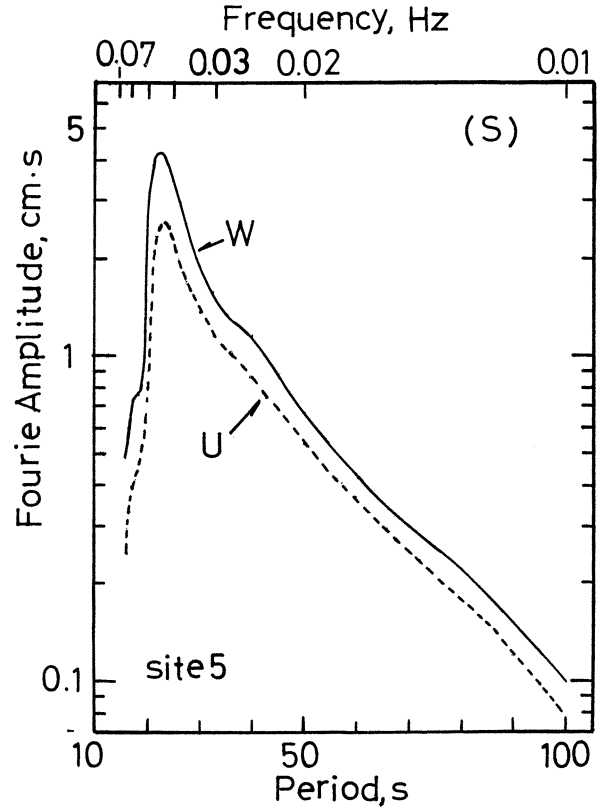

Fig. 2. (a) Fourier spectra of incident Rayleigh waves. The waves were calculated for the 3-D stratified medium (Model S) at site 5.

tain foot at site 5, calculated for Models LB and T, are shown in Fig. 2 b. Initial values calculated for Model S consist only of the W- and U-components, as described in section 2. However, site 5 is already involved inside the inhomogeneous wave guide; thus, the wavetrains at site 5 include a small amount of the V-component due to effects of the scattering of incident waves.

Transmitted waves of the W-, U-, and V-components recorded at site 15′ are shown in Fig. 3. The figure clearly shows that the amplitudes of the V-component are stronger for Model LB than for Model T for both of $\phi = 30°$ and 60°. Fourier spectral amplitudes of the waves of the three components are calculated and shown in Fig. 4. We can see the spectral characteristics of the V-component in detail in the figure: The amplitudes of the V-component for Model LB are larger than those for Model T in a wide period range of 20–70 s for both the azimuthal angles of incidence; the spectral peaks of the V-component, as well as those of the W- and the U-components, are located near 23 s; the predominant periods are consis-
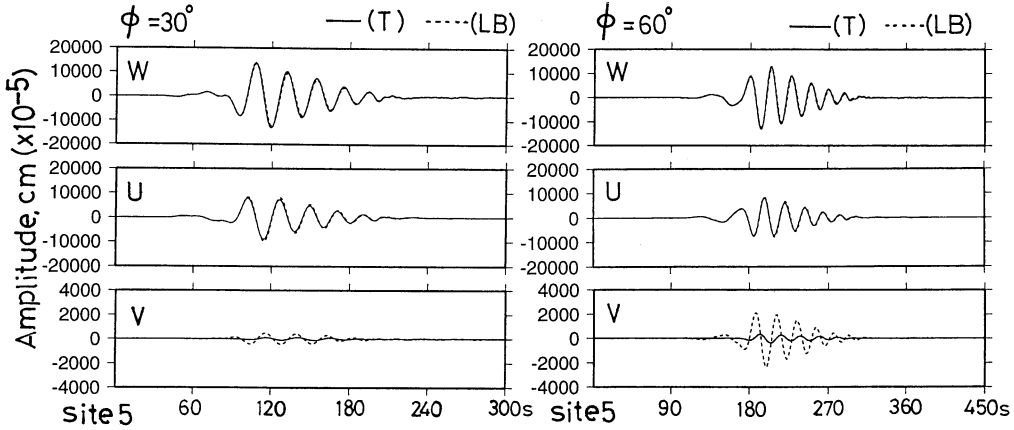
Fig. 2.(b) Waveforms of the vertical (W), radial (U), and transverse (V) components at site 5 for the azimuthal angles of incidence of 30 (left) and 60 (right) degs. The waveforms for Models T and LB are traced by solid and dotted lines, respectively.
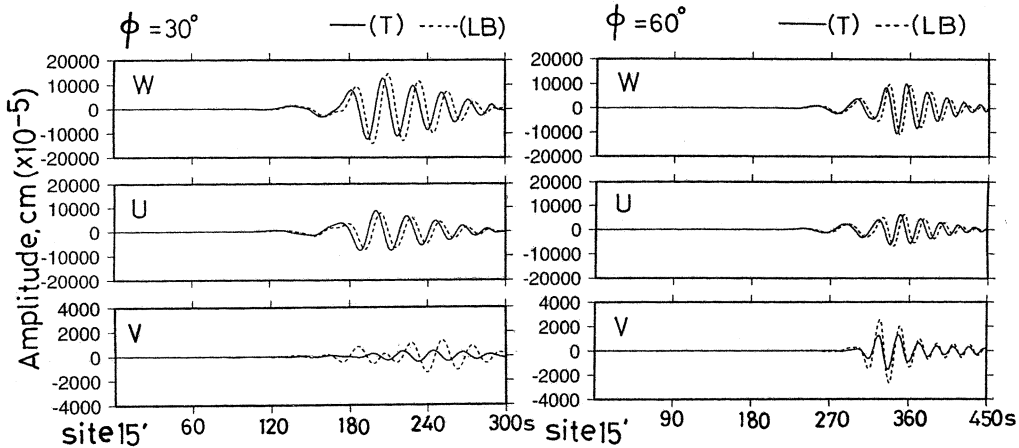

Fig. 3. Legend as for Fig. 2b except for site 15′.

tent with those of incident Rayleigh waves of the W- and the U-components (Fig. 2 a).

　These spectral features suggest that incident Rayleigh waves of periods of 20–50 s with large amplitudes are efficiently converted to Love waves in the Tien Shan, especially for Model LB. The high conversion from P-SV waves (Rayleigh waves) to SH-waves (Love waves) near the period range might be caused by the existence of a double LVZ located in the lower crust and the upper mantle. However, it is noted that the amplitudes of the V-component are lower than those of the W- and the U-component.

4. Rate of conversion from Rayleigh to Love waves

　In this section we evaluate the maximum rate of conversion from Rayleigh to Love waves for the eastern and western regions of the Tien Shan and compare it with the results of Pedersen *et al.* (1998). Here, we temporarily define the rate of conversion from Rayleigh to Love waves as the "spectral amplitude ratio of the transverse (V) component at wave's retreat edge (site 15′) of the mountain to the vertical (W) component at wave's approach edge (site 5) of the mountain". The ratios, calculated using the wave trains given in Figs. 2 and 3, are shown in Figs. 5 and 6. The ratios are determined for two upper mantle shear wave velocities (Vs) of 4.9 and 4.6 km/s, with other physical parameters fixed to ones described in section 2. As described in detail in section 6, the Vs of 4.6 and 4.9 km/s in the upper mantle is close to that of the eastern and western regions of the Tien Shan, respectively. The Vs of 4.9 km/s, which was used by Pedersen *et al.* (1998) and paper I, is somewhat high
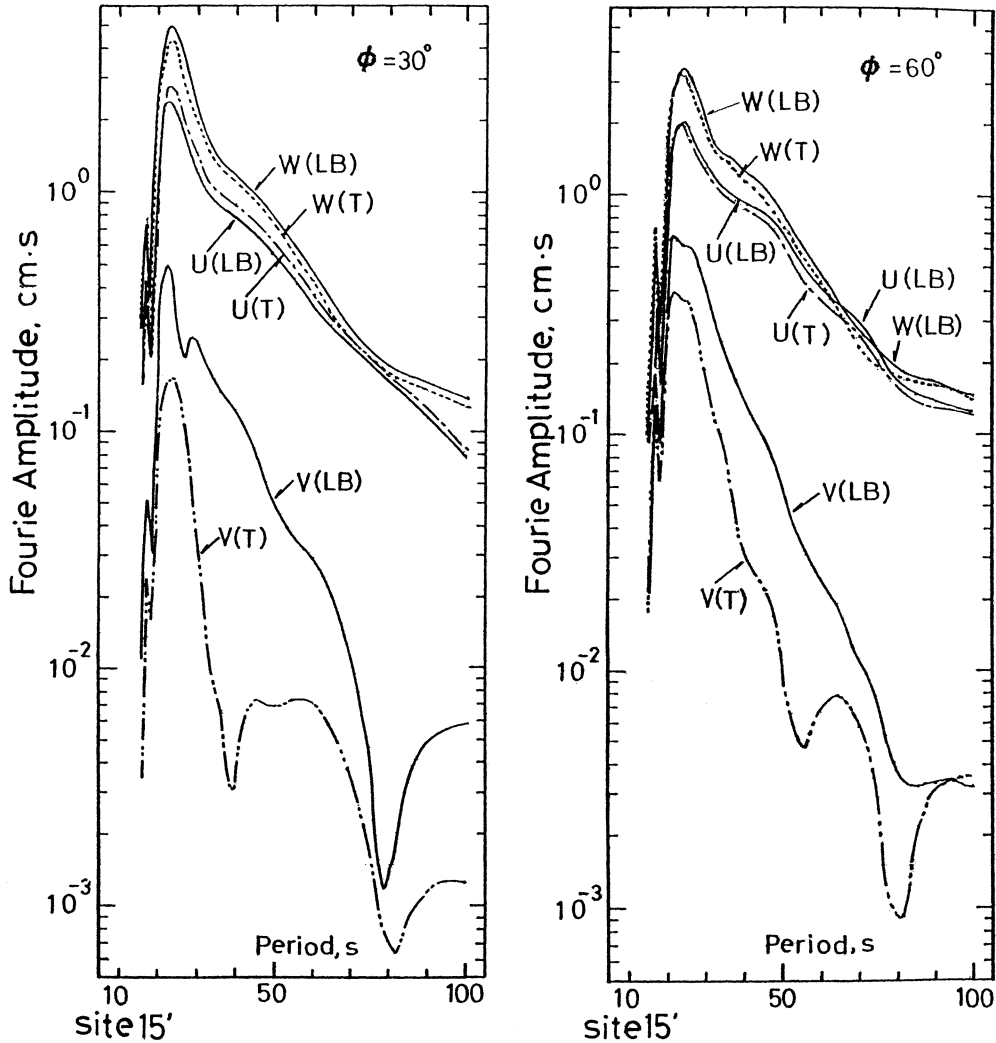
Fig. 4. Spectral amplitudes of the vertical (W), radial (U), and transverse (V) components at site 15′ for Models LB and T and for the azimuthal angles of incidence of 30 (left) and 60 (right) degs.

(the Poisson ratio is 0.19). The Vs of 4.6 km/s were determined by Cotton and Avouac (1994) using surface wave data (the Poisson ratio is 0.24).

The notable features of the ratios can be extracted from Fig. 5:

4-1) The rate is a maximum of 0.3 for Model LB in a period range of 15–20 s for $\phi = 60°$ for both of Vs =4.9 and 4.6 km/s; the rate decreases with an increase in period from 20 to 70 s.

4-2) The rate is smaller for Vs=4.6 km/s than for Vs=4.9 km/s for priods of 20–70 s, as far as the azimuthal angle of incidence is the same in the cases of oblique incidence.

4-3) The maxmum rates for Model T are smaller than those for Model LB, by about 0.1 for both ϕ=30° and 60°, and the rates for Model T are significantly

smaller than those for Model LB for periods longer than 30 s.

The features 4-1), and 4-2) indicate that the maximum rate of 0.3 for Model LB is slightly lower than that of about 0.34 obtained by Pedersen *et al.* (1998, Fig. 15) for a mountain model including a small size LVZ at the bottom of the mountain. This can be attributed to the horizontal length of the mountain root in their model being approximately 300 km, which is wider by about 50 km than that assumed in the present model. They simulated wavetrains using the indirect boundary element method and determined the rate of conversion from spectral ratios of the V-component at wave's retreat site of the mountain over the W-component at wave's approach site of the mountain. The distance between the two sites
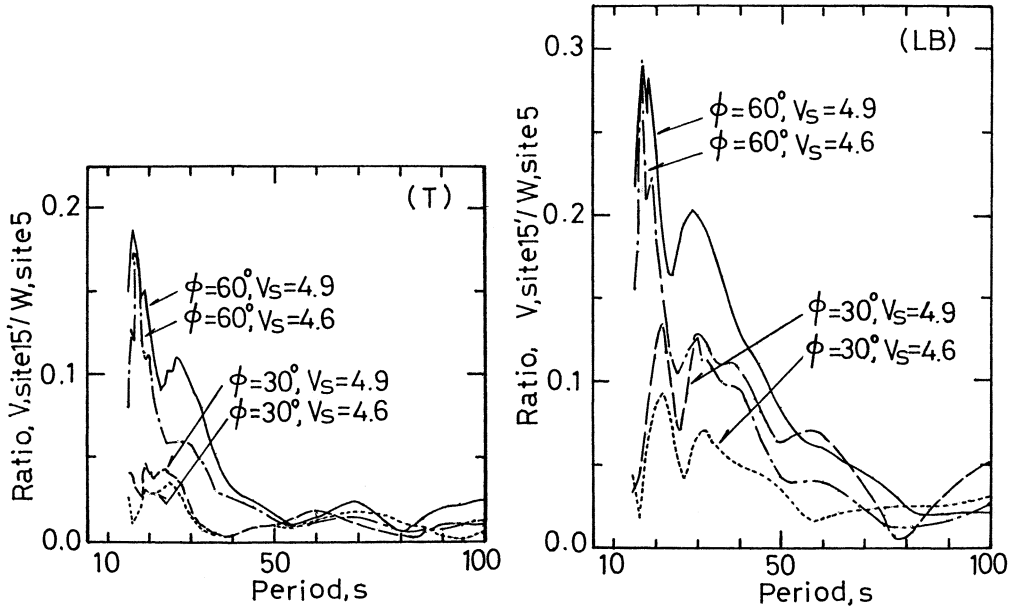
Fig. 5. Spectral amplitude ratios of the V-component at site 15′ and the W-component at site 5. The ratios are calculated for Models T (left) and LB (right) for cases of (1) mantle shear wave velocities of Vs=4.6 and 4.9 km/s and (2) azimuthal angles of incidence of ϕ=30 and 60 degs.

is 1500 km wide. However, the mountain area with significant crustal thickening is only 300 km wide inside the path, the maximum crustal thickness being 55 km. So, the ratios they obtained are comparable to ones determined in the present work, because the background structure and the mountain structure are very similar to each other. It is noted here that the azimuth of ϕ=60°, assumed in the calculation, is larger than those assumed by Pedersen *et al.* (1998). They showed that the azimuth increase generally induces an increase in Love wave amplitudes for ϕ=10°–50°. The feature 4–3) can be attributed to the greater generation of scattered waves with longer wavelengths for Model LB than for Model T (see also Appendix).

In order to determine the difference in amplitude between the V- and the W-components recorded at "one station" located at the wave's retreat edge (site 15′), the ratios of amplitudes of the V-component and those of the W-component at site 15′ for Model LB were calculated as shown in Fig. 6. The ratios for ϕ= 60° show maxima of 0.4 near 20 s, which are higher by about 0.1 than those obtained on the basis of the definition of the rate of conversion (Fig. 5). The maximum ratios of about 0.11 and 0.08 for ϕ=30°, for Vs=4.9 and 4.6 km/s, respectively, are slightly lower than those in Fig. 5. But, the general pattern of
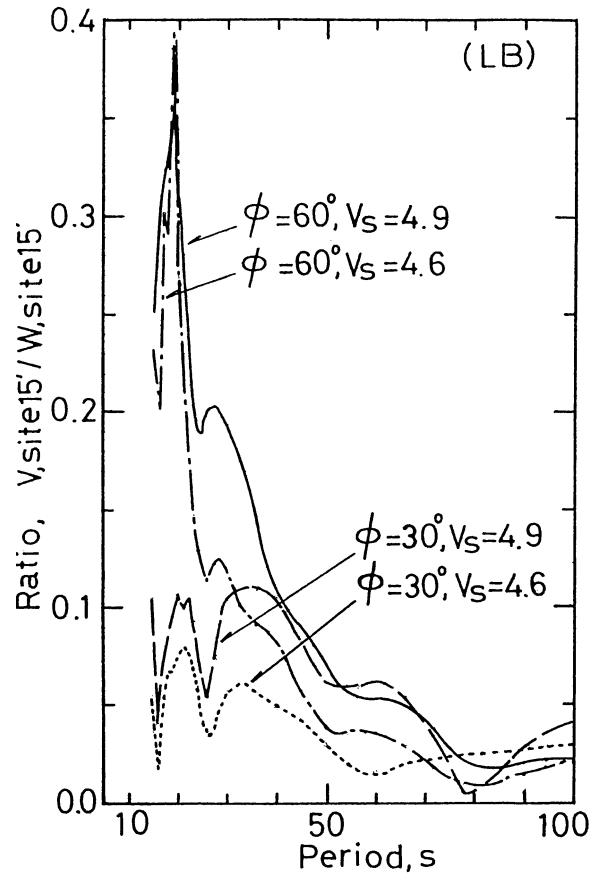

Fig. 6. Spectral amplitude ratios of the V-component at site 15′ and the W-component at site 15′. The ratios are calculated for Model LB.

spectral ratios given in Fig. 6 is similar to that for Model LB in Fig. 5. The high maximum ratios of 0.4 near 20 s for $\phi=60°$, mentioned above, are caused by very low transmission coefficients of the W-component at site 15′ (Fig. 7). Here, the transmission coefficient is defined as the spectral amplitude ratio of the W-component at site 15′ for Model LB and the one for the stratified medium (Model S). In Fig. 7, the transmission coefficients for the U-component are also shown for reference.

The overall characteristics of the rates of conversion featured above indicate that the maximum rates are less than 0.4, even if the large-scale double LVZ exists beneath the Tien Shan; the rates are too low to explain large amplitudes of observed Love waves (Pedersen *et al.* 1998, Fig. 4) due to the Lop Nor nuclear test, the amplitudes being equal to or greater than those of Rayleigh waves.

It is suggested in section 6 that the rates of conversion would increase more than those estimated above if we take into consideration the actual complicated geometry of the Tien Shan. So, the observed strong Love waves might be generated by the conversion from Rayleigh to Love waves in the

propagation process over the actual complicated Tien Shan mountain range and/or by a tectonic release near the test site, as demonstrated by Levshin and Ritswoller (1995) from the study of group velocities of Rayleigh and Love waves due to the Lop Nor nuclear test.

5. Variation of wave energy

Converted Love waves are generated at the expense of the wave energy of Rayleigh waves. This means that the wave energy of Rayleigh waves of the W- and the U-components decreases during propagation over the Tien Shan. This problem has not been investigated yet from observed surface waves. In this section we try to clarify how the wave energy of incident waves varies in the propagation process through the Tien Shan, using wavetrains recorded at the free surface on the great circle.

In the present work, the medium is assumed to be a perfectly elastic body, and a plane Rayleigh wave incidence on the elastic body is assumed. Thus, there is no energy loss in the propagation of surface waves in the stratified medium. Here, we examine the variation of wave energy in the propagation
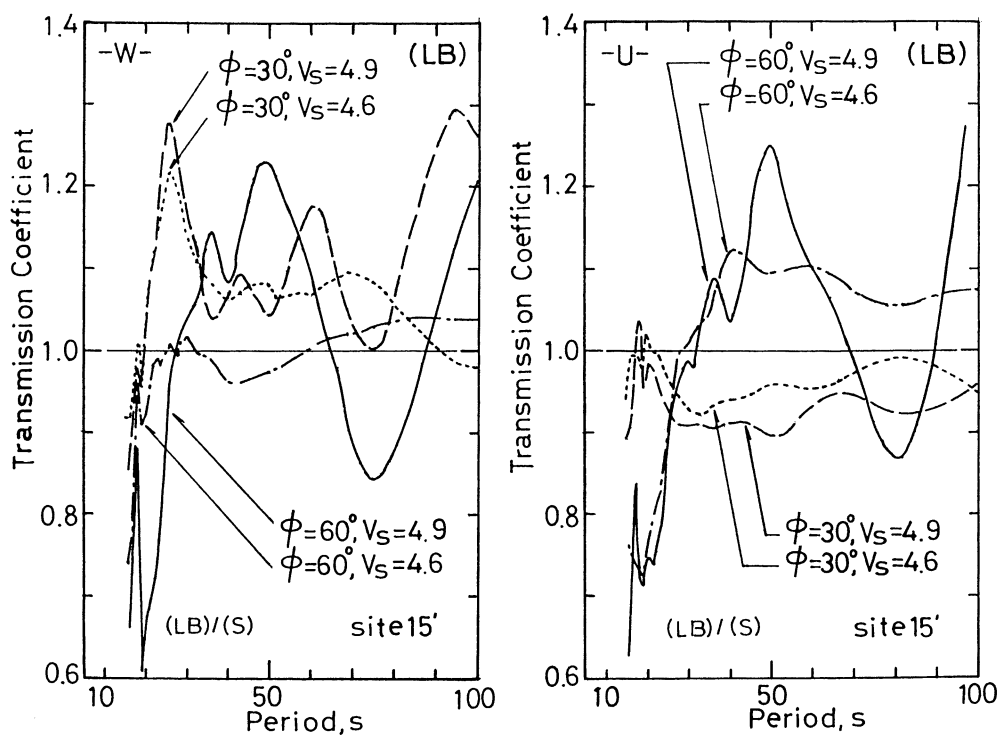

Fig. 7. Transmission coefficients of the W- and the U- components for Model LB. The coefficients are calculated from the spectral amplitude ratios of the W-components at site 15′ for Models LB and those for Model S.

process in the media with or without a mountain root structure, or in the media with or without a large-scale double LVZ beneath the mountain.

5. 1 Definition of wave energy

According to Parseval's theorem, the integration of the square of a real time function f (t) is equivalent to the integration of the square of a Fourier transform F (ω) of f (t):

$$\int^{\infty}_{-\infty}[f(t)]^2 dt = 2 \int^{\infty}_{0}|F(\omega)|^2 d\nu, \qquad (9)$$

where $\nu = \omega/2\pi$ is the frequency. The function $2|F(\omega)|^2$ is called the spectral energy density (e.g., Ben-Menahem and Shingh, 1981: pp. 247, Eq. (4.275)). Using the expression (9) we temporarily define the wave energy of propagating waves as the sum of the square of the time function of the vertical (W), the radial (U), and the transverse (V) components in the following form:

$$\Sigma W^2(j)\Delta t(\Delta t=0.3) = \int^{450}_{0}[W(t)]^2 dt,$$
$$\Sigma U^2(j)\Delta t(\Delta t=0.3) = \int^{450}_{0}[U(t)]^2 dt, \qquad (10)$$
$$\Sigma V^2(j)\Delta t(\Delta t=0.3) = \int^{450}_{0}[V(t)]^2 dt,$$

where j is the data point number (j=1-1500) and t is the sampling time (t=0-450). Eq. (10) indicates that the wave energy is proportional to the square of the amplitudes of the time function.

5.2 Characteristics of wave energy

We evaluated the wave energy of incident and transmitted waves recorded at sites 5 and 15′ on the great circle, respectively, by calculating the cumulative distributions of the square of amplitudes of the wavetrains for Models T and LB (Figs. 8 and 9). The computations were also done for the stratified medium (Model S) in order to verify the accuracy of energy propagation (Fig. 10). Two different shear wave velocities of Vs=4.6 and 4.9 km/s in the upper mantle were used for the calculation of the wave energy, as well as done for the calculation of the rate of conversion. In the following, the percentage associated with the wave energy is determined using numerical values at a computation time of 450 s in Figs. 8, 9, and 10. Several features can be verified through the figures (Figs. 8 and 9):

5-1) For Model LB, the wave energy of the V-component at site 15′ is about 82% of that at site 5 for Vs=4.6 km/s, but about 106% for Vs=4.9 km/s.

5-2) For Models LB and T with Vs=4.9 km/s, the total wave energies of three components at site 15′ are about 70 and 75% of those at site 5, respectively. But the respective total energies are about 77% of
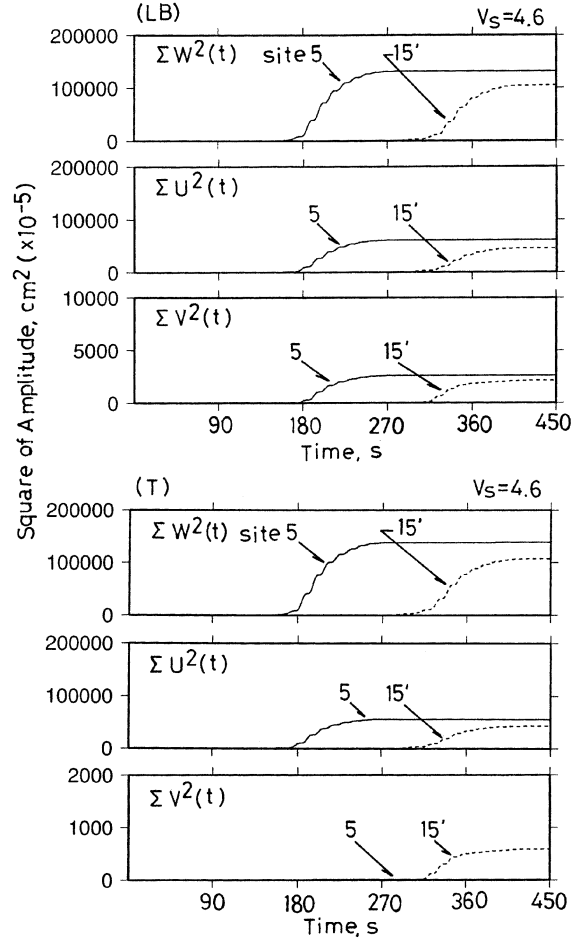

Fig. 8. Cumulative distributions of the square of amplitudes of incident (site 5) and transmitted (site 15′) waves of the W-, U-, and V-components. The distributions are determined for 3-D Models LB (top) and T (bottom) with a mantle shear wave velocity of Vs=4.6 km/s. The azimuthal angle of incidence is assumed to be 60 deg.

those for both Models LB and T with Vs=4.6 km/s.

5-3) For Model T, the wave energy of the V-component at site 15′ is much higher than that at site 5. This characteristic does not depend on the shear wave velocity in the upper mantle.

5-4) For Model T, the ratios (15′/5) of both the W- and the U-components for Vs=4.6 and 4.9 km/s are about 77 and 70%, respectively.

The features 5-2) and 5-4) indicate that the decrease of the wave energy of Rayleigh waves across the Tien Shan is greater for the western region than for the eastern region. According to body wave studies (Kosarev *et al.* (1993)), there are some regions where the LVZ is not detected in the crust. Using features 5-1) and 5-3) it may be possible to distin-
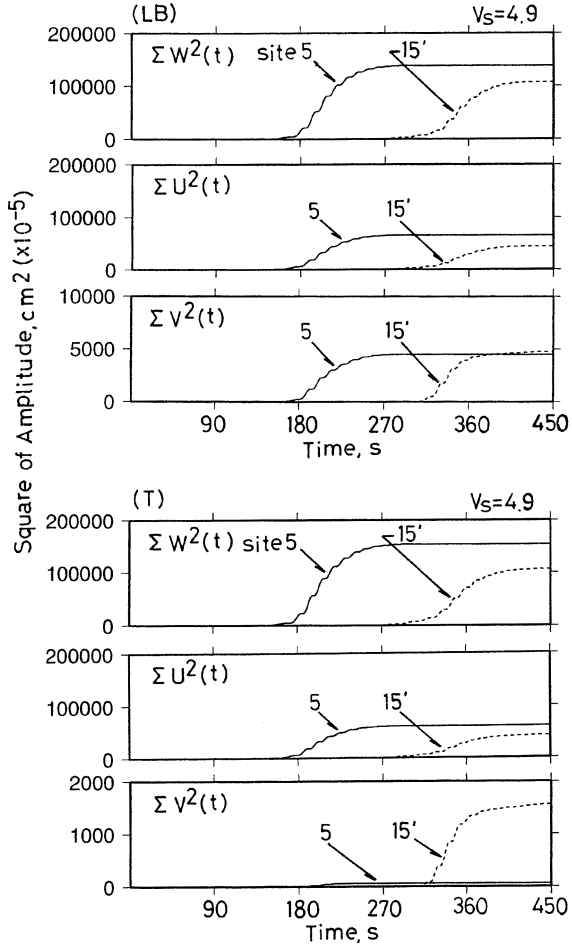
Fig. 9. Legend as for Fig. 8 except for a mantle shear wave velocity of Vs= 4.9 km/s.

Fig. 10. Legend as for Fig. 8 except for a 3-D stratified medium (Model S) with mantle shear wave velocities of Vs=4.9 (top) and 4.6 (bottom) km/s. The location of site 15′ corresponds to that for $\phi=60°$.

guish whether or not the LVZ is involved beneath those regions. These characteristics will be verified if the analyses of observed surface waves advance in the future.

The large decrease of the wave energy of transmitted waves of the W- and the U-components for Vs =4.9 km/s suggests that scattered waves, which were produced near the mountain root boundaries and dissipate all around, are predominant due to the large contrast in the acoustic impedence between the crust and the upper mantle.

For Model S, which is the 3-D stratified medium, sites 5 and 15′ in Fig. 10 merely correspond to the locations with a path length of 500 km between the two stations, equivalent to the length for Models T and LB for $\phi=60°$. In this case, the wave energies of the W- and the U-components at site 15′ are equal to those of the respective components at site 5. Namely, the total wave energy of incident Rayleigh waves,
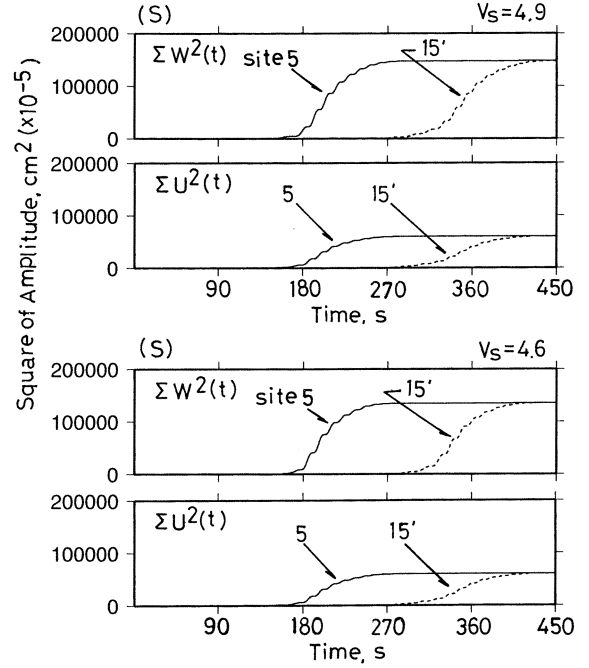
the sum of the two components recorded at site 5, is consistent with that of transmitted waves recorded at site 15′. The error is within 0.4–0.5%. This result guarantees the accuracy of the calculations, done by the present method of plane Rayleigh wave incidence.

6. Applicability of mountain model

According to Kosarev et al. (1993) the crustal and upper mantle structures in the Tien Shan are significantly different on either side of the Talasso Fergana fault, which is located at the western part of the Tien Shan, trending northwest-southeast (Fig. 11). It is shown from teleseismic earthquake arrival times (Vinnik and Saipbekova, 1984) that P-wave velocities in the upper mantle are anomalously low (7.7 km/s) east of the fault and anomalously high (8.4 km/s) west of it, and that on average the crustal velocities to the east are lower than those to the west. The crustal model parameters used in the present work correspond to the average ones for the Tien shan (Pedersen et al., 1998), which are based on Burov et al. (1990), Avouac et al. (1993), Kosarev et al. (1993) and Cotton and Avouac (1994). However, the shear wave
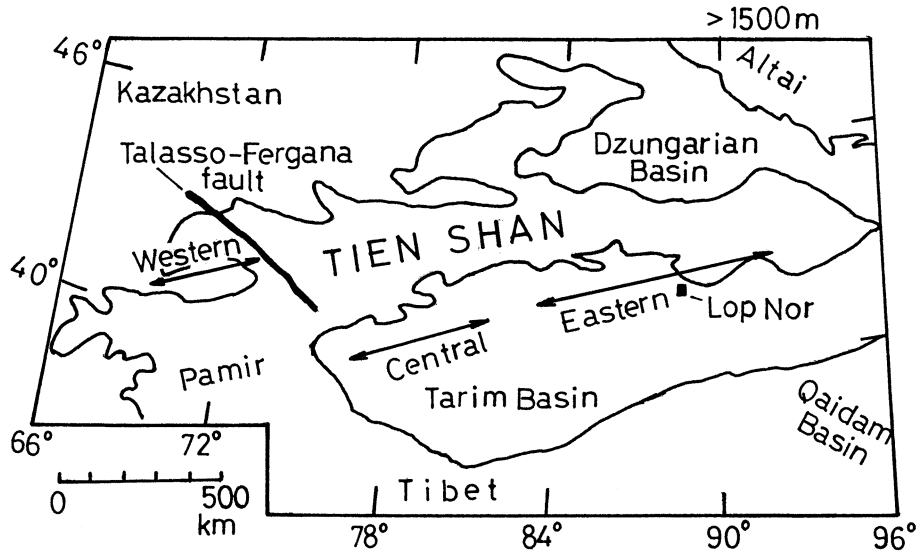
Fig. 11. Schematic map of the Tien Shan with elevations of more than about 1500 m. Lop Nor
is the nuclear test site (modified from Cotton and Avouac (1994), Avouac *et al.* (1993), and
Kosarev *et al* (1993)).

velocities of Vs＝4.6 and 4.9 km/s in the upper mantle
are rather close to those of the eastern and western
parts of the Talasso Fergana fault, respectively (Ko-
sarev *et al.*, 1993). So, the results obtained for Vs＝4.6
km/s correspond to approximately to the regions of
the eastern Tien Shan and the central Tien Shan, east
of the Talasso Fergana fault, and the results for Vs＝
4.9 km/s correspond to the region of the western Tien
Shan, west of the fault.

The most significant feature of the structure
beneath the Tien Shan is the existence of a large-
scale double LVZ in the lower crust and in the upper
mantle (Cotton and Avouac, 1994). It is inferred that
the upper mantle beneath the Tien Shan east of the
Talasso Fergana fault is partially melted, and low
velocities in the lower crust could be due to vertical
intrusions of mantle materials (Kosarev *et al.*, 1994).
Love waves converted from Rayleigh waves at
wave's approach edge of the mountain, whose energy
is comparable or beyond the one at wave's retreat
edge of the mountain, as shown for Models LB in
Figs. 8 and 9, can be produced only at these peculiar
structures with a prominently developed large-scale
double LVZ. The geometry of the Tien Shan is very
complicated, as shown in Fig. 11. When Rayleigh
waves, excited by Nuclear explosion detonated at the
Lop Nor test site, travel in the northwestern direc-
tion, the multiple interferences between incident
Rayleigh waves and converted Love waves are ex-

pected to successfully occur because propagating
waves cross the curved peripheries of the Tien Shan
more than twice. Furthermore, the Love waves can
be greatly amplified if surface waves are generated
by the teconic release near the test site, as suggested
in section 4.

7. Conclusion

Surface wave interconversion in the Tien Shan-
like mountain root strcuture in China was investi-
gated though 3-D numerical simulations, taking into
account the oblique incidence of plane Rayleigh
waves on the mountain range. Striking features of
the mountain model analyzed include the existence
of a large-scale double LVZ in the lower crust and in
the upper mantle located at depths of 37.5–52.5 km
and 112.5–162.5 km, respectively. The horizontal
scale of the 2-D mountain root has a length of 250 km,
which is slightly less than the actual one of 300 km.

In the cases of the azimuthal angles of incidence
of 30° and 60° in the 3-D simulations, the path lengths
along the great circle are assumed to be about 290
and 500 km, respectively. The characteristics of sur-
face wave interconversion elucidated in the present
Tien Shan model are considererd to present a lower
estimation of the rate of conversion fom Rayleigh to
Love waves for periods of 16–90 s. The main findings
include the determination of maximum rates of con-
version of 0.3–0.4 near 20 s for the azimuthal angle of

incidence of $60°$; these maximum rates are not so different from those previously estimated by Pedersen *et al.* (1998), and are too low to explain the observation of large amplitudes of Love waves due to the Lop Nor nuclear explosions. These results suggest that the observed large amplitude Love waves might be generated by the amplification of converted Love waves due to the complicated geometry of the Tien Shan range, which is not taken into consideration in the present model and/or by the tectonic release near the nuclear test site.

With respect to the wave energy, the following results associated with mantle shear wave velocity-dependence were obtained: The mantle shear wave velocities of 4.6 and 4.9 km/s correspond approximately to the region of the eastern and central Tien Shan, east of the Talasso Fergana fault and to the region of the western Tien Shan, west of it, respectively. For the mountain model with the double LVZ, the wave energy of the transverse component at wave's retreat edge of the mountain is relatively smaller than that at wave's approach edge of the mountain in the case of the mantle shear wave velocity of 4.6 km/s; Namely, the former is about 82% of the latter, but about 106% for the mantle shear wave velocity of 4.9 km/s. For the mountain models with and without the double LVZ, the total wave energies of the vertical, the radial, and the transverse components at wave's retreat site of the mountain are about 70 and 75% of those at wave's approach site of the mountain, respectively, for the mantle shear wave velocity of 4.9 km/s. However, the respective total wave energies are about 77% of those for the mantle shear wave velocity of 4.6 km/s; for the mountain model without the double LVZ, the wave energy of the transverse component at wave's retreat site of the mountain is much higher than that at wave's approach site of the mountain and this property does not depend on the shear wave velocity in the mantle.

Several of the characteristics deduced above will be useful for more rigorously imaging the polarization anomaly of surface waves across the Tien Shan and for more precisely determining the crustal and upper mantle structures of the Tien Shan. In the present paper, the wave energies of surface waves at the free surface were discussed. The evaluations of surface wave energies in the crust and the upper mantle, as well as those of body wave energies radi-ated into the inner parts of the earth, are future subjects of our research.

References

Aki, K. and P.G. Richard, 1980, Quantitative seismology: Theory and method, Vol. II, pp. 779–780, W.H. Freeman and Company, San Francisco.

Avouac, J.P., P. Tapponnier, M. Bai, H. You and G. Wang, 1993, Active faulting and folding in the northern Tien Shan and rotation of Tarim relative to Dzungaria and Kazakhstan, *J. Geophys. Res.,* **98**, 6755–6804.

Ben-Menahem, A. and S.J. Singh, 1981, Seismic waves and sources, pp. 246–247, Springer-Verlag New York Inc.

Boore, D.M., 1970, Love waves in nonuniform wave guide: Finite difference calculations, *J. Geophys. Res.,* **75**, 1512–1527.

Burov, E.V., Kogan, M.G., Lyon-Caen, H. and P. Molnar., 1990, Gravity anomalies, the deep structures, and dynamic process beneath the Tien Shan, *Earth Planet. Sci. Lett.,* **96**, 367–383.

Chang, W.F. and G.A. McMechan, 1989, Absorbing boundary condition for 3-D acoustic and elastic finite-difference calculations, *Bull. Seism. Soc. Am.,* **79**, 211–218.

Clayton, R. and B. Engquist, 1977, Absorbing boundary conditions for acoustic and elastic equations, *Bull. Seism. Soc. Am.,* **67**, 1529–1540.

Cotton, F. and J.P. Avouac, 1994, crustal and upper-mantle structures under the Tien Shan from surface-wave dispersion, *Phys. Earth Planet. Inter.,* **84**, 95–109.

Frankel, A. and J. Vidale, 1992, A three-dimensional simulation of seismic waves in the Santa Clara valley, California, from a Loma Prieta aftershock, *Bull. Seism. Soc. Am.,* **82**, 2045–2074.

Gregersen, S., 1978, Possible mode conversion between Love and Rayleigh waves at a continental margin, *Geophys. J.R. Astr. Soc.,* **54**, 121–127.

Kosarev, G.L., N.V. Petersen, L.P. Vinnik and S.W. Roecker, 1993, Receiver function for the Tien Shan analog broad-band networks: Contracts in the evolution of stuctures across the Talasso-Fergana faults, *J. Geophys. Res.,* **98**, 4437–4449.

Levshin, A., L. and M.H. Ritzwoller, 1995, Characteristics of surface waves generated by events on and near the Chinese nuclear test site, *Geophys. J. Int.,* **123**, 131–148.

Malischewsky, P., 1976, Surface waves in media having lateral inhomogeneities, *Pure and Applied Geophysics,*

114, 833–843.

Malischewsky, P., 1987, Surface waves and discontinuities, Elsevier, Amstedam.

Malischewsky, P., 2000, Some special solutions of Rayleigh's equation and the reflection of body waves at a free surface, *Geofisical Internacional,* **39**, 2, 155–160.

Maupin, V., 1996, The radiation modes of a vertically varying half-space : a new representation of the complete Green's function in terms of modes, *Geophys. J. Int.,* **126**, 762–780.

Mikumo, T., K. Hirahara and T. Miyatake, 1987, Dynamical fault rapture process in heterogeneous media, *Tectonophys.,* **144**, 19–36.

Momoi, T., 1987, Scattering of Rayleigh waves by a semi-circular rough surface on a layered media, *Bull. Earthq. Res. Inst., Univ. Tokyo,* **62**, 163–200.

Pedersen, H.A., J.P. Avouac and M. Campillo, 1998, Anoma-lous surface waves from Lop Nor nuclear explosions: Observations and numerical modeling, *J. Geophys. Res.,* **103**, 15051–15068.

Vinnik, L.P. and A.M. Saipbekova, 1984, Structure of the lithosphere and the asthenosphere of the Tien Shan, *Ann. Geophys.,* **2** (6), 621–626.

Yomogida, K. and J.T. Etgen, 1993, 3-D wave propagation in the Los Angel Basin for the Whittier-Narrows earthquake, *Bull. Seism. Soc. Am.,* **83**, 1325–1344.

Yoshida, M., 1999, 2-D wave fields of Love wave propagation through a continental crust with a dent, *Zisin* 2, **51**, 367–378 (in Japanese with English abstract).

Yoshida, M., 2001, Oscillation of a mountain root structure due to a Rayleigh wave incidence, *Earth Planets Space,* **53**, 1099–1109.

Appendix

In this appendix, the wavefields of scattered waves (Sc) of the W-component for 2-D Models T and LB are shown for various instants in time from T=25 to 250 s at every 25 s. The snapshots of the displacements of scattered waves at surface z=0 are given at the respective times in Fig. 6 (a) of paper I. The scattered waves are generated during the propagation of incident plane Rayleigh waves, similar to those shown in Fig. 2, through the computational space including a mountain root structure located between sites 5 and 15 with (Model LB) or without (Model T) a double LVZ beneath it. The scattered waves are obtained from the expression Sc (t, x, z)= En (t, x, z)−Pr (t, x, z) (Aki and Richard, 1980). The entire (En) and primary (Pr) waves are calculated for the nonuniform and uniform wave guides, respectively. The computational space has a horizontal length of 1000 km and a vertical depth of 500 km. The snapshots of the wavefields of the scattered waves indicate following features: the phases of the scattered waves vary concentrically in the substratum; the wavelengths of the scattered waves for Model LB are longer than those for Model T (Figs. A1(a) and A 2(a)); and, the scattered waves are generated at deeper parts for Model LB than for Model T (Figs. A 1 (b) and A2 (b), especially at T=25, 50, and 75 s). In the case of 3-D problems regarding the oblique incidence of Rayleigh waves, the energy of the scattered waves of the W-component, whose distributions might be similar to those shown in Figs. A1 (b) and A 2 (b), can be partitioned mostly into transmitted waves and partly into reflected waves, converted Love waves, and body waves penetrating into the mantle.
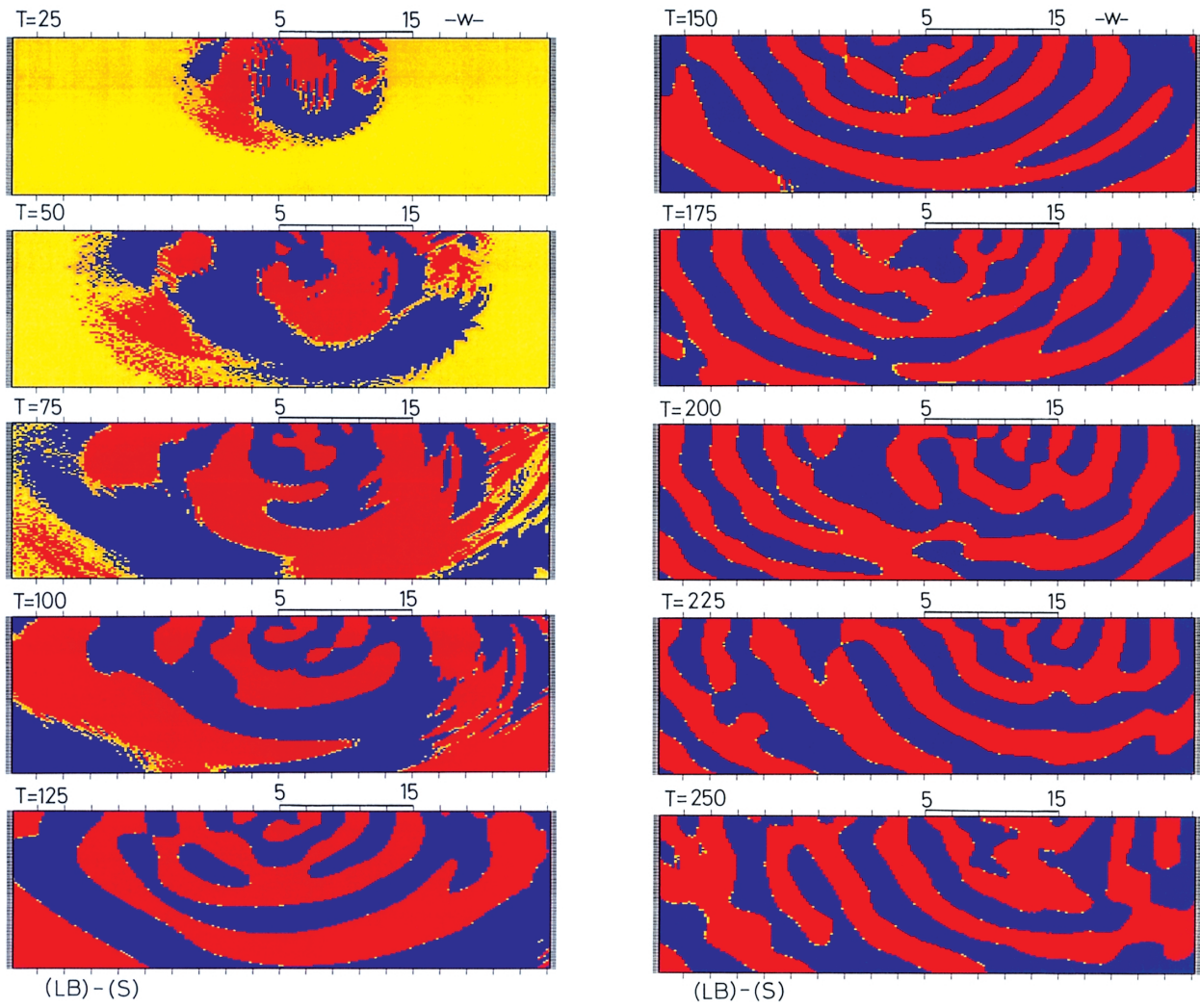
Fig. A1(a). The phase distributions of the displacement of the vertical component of the scattered waves for 2-D Model LB at various instants in time (T) from 25 to 250 s. The positive and negative components of the displacement are shown by blue and red colors, respectively.
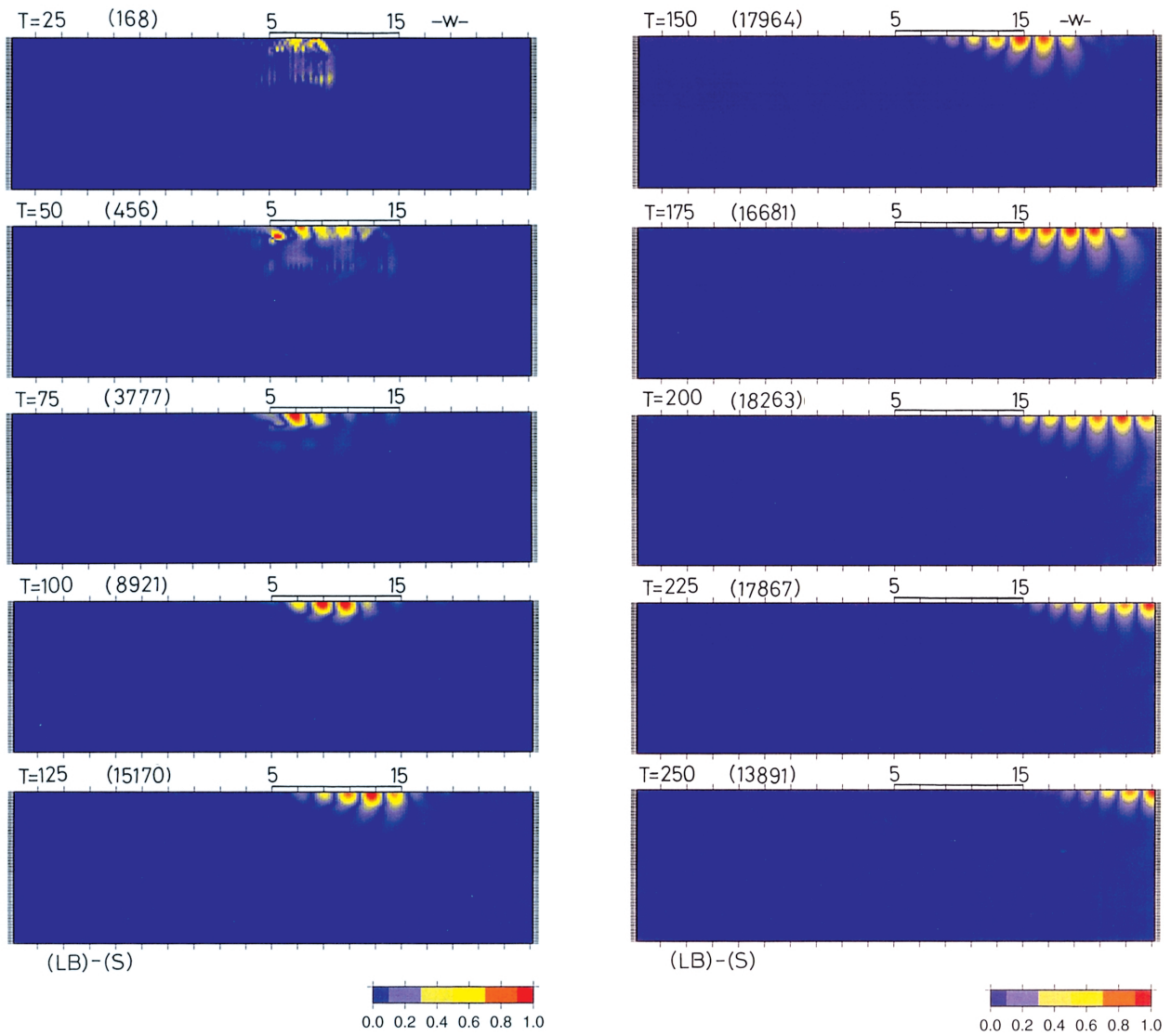
Fig. A1(b). The amplitude distributions of the displacement of the vertical component of the scattered waves for 2-D Model LB at various instants in time (T) from 25 to 250 s. The amplitude is normalized by a maximum displacement at time T, with the maximum given in parentheses on a relative scale.
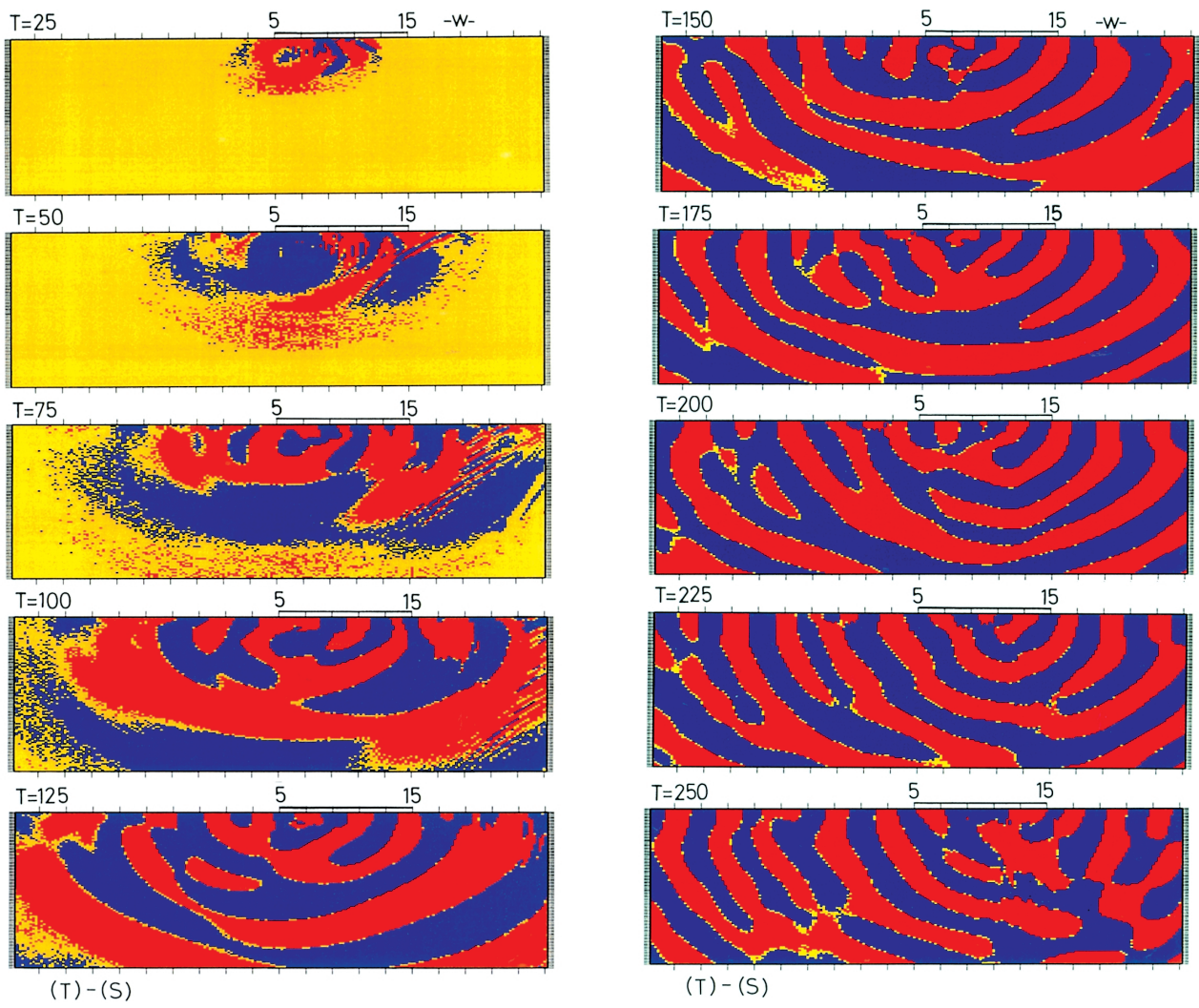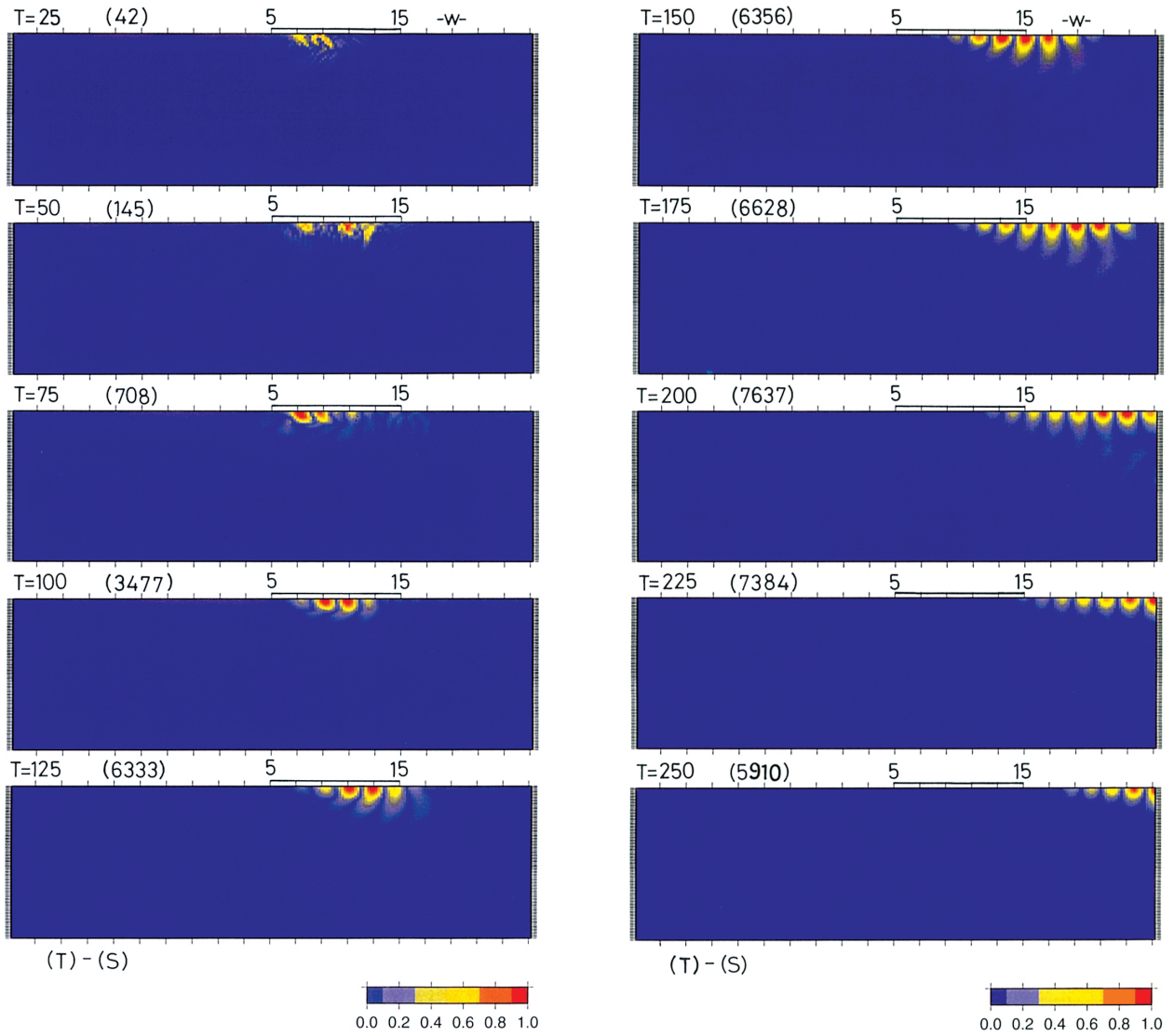
Fig. A2(a). Legend as for Fig. A1 (a) except for 2-D Model T.

Fig. A2(b). Legend as for Fig. A1 (b) except for 2-D Model T.